



Agitation drying synthesis of porous carbon supported Li_3VO_4 as advanced anode material for lithium-ion batteries

Wen-Wen Gou, Shuang Zhou, Xin-Xin Cao*[✉], Yi-Lin Luo, Xiang-Zhong Kong, Jing Chen, Xue-Fang Xie, An-Qiang Pan*[✉]

Received: 12 June 2020 / Revised: 3 November 2020 / Accepted: 20 January 2021 / Published online: 21 April 2021
© Youke Publishing Co., Ltd. 2021

Abstract Li_3VO_4 has been considered as a promising insertion-type anode for lithium-ion batteries due to its high theoretical specific capacity and suitable operating voltage platform. However, this promising anode still suffers from poor electrical conductivity. To address this issue, herein, a porous carbon supported Li_3VO_4 composites ($\text{Li}_3\text{VO}_4/\text{C}$) via a facile agitation-drying method combined with subsequent calcination is reported, in which Ketjen black carbon with high porosity, easy dispersion and excellent conductivity can serve as one of carbon

sources. The $\text{Li}_3\text{VO}_4/\text{C}$ composite prepared at 700 °C with a carbon content of ~ 10% exhibits the optimized structure. The void space of the composite accommodates the volume changes during the charge/discharge process. Meanwhile, the carbon shell serves as a conductive skeleton to provide bi-continuous Li ions and electrons pathways. Electrochemical results reveal that the composite delivers a high initial discharge capacity of 572 $\text{mAh}\cdot\text{g}^{-1}$ and maintains a capacity of 442.9 $\text{mAh}\cdot\text{g}^{-1}$ after 100 cycles at 100 $\text{mA}\cdot\text{g}^{-1}$. Even at a high current density of 2 $\text{A}\cdot\text{g}^{-1}$, a considerable capacity of 243.8 $\text{mAh}\cdot\text{g}^{-1}$ can still be obtained. This work provides a promising approach for the practical application of Li_3VO_4 as anode material for LIBs.

Wen-Wen Gou and Shuang Zhou have contributed equally to this work

Supplementary information The online version contains supplementary material available at (<https://doi.org/10.1007/s12598-021-01712-5>).

W.-W. Gou, S. Zhou, X.-X. Cao*, Y.-L. Luo, J. Chen, X.-F. Xie, A.-Q. Pan*
School of Materials Science and Engineering, Central South University, Changsha 410083, China
e-mail: caoxinxin@csu.edu.cn

A.-Q. Pan
e-mail: pananqiang@csu.edu.cn

X.-Z. Kong
Institute of New Energy, College of Mechanical Engineering, Hunan Institute of Science and Technology, Yueyang 414006, China

A.-Q. Pan
Key Laboratory of Advanced Energy Materials Chemistry (Ministry of Education), Nankai University, Tianjin 300071, China

A.-Q. Pan
School of Physics and Technology, Xinjiang University, Urumqi 830046, China

Keywords Lithium-ion battery; Anode; Li_3VO_4 ; Ketjen black carbon; Electrochemical performance

1 Introduction

Lithium-ion batteries (LIBs) have achieved great successes as power supplier in high-tech electronic devices and electrical vehicles due to their high energy density and good environmental benignity [1–3]. However, the relatively low power density arising from the slow diffusion of Li ions within the electrode materials stimulates the search of new electrode materials to fulfill the increasing requirements of customers [4, 5]. In particular, anode materials, as a key component of LIBs, greatly affect the electrochemical properties of LIBs. The development and exploration of advanced anode materials is crucial to solving this problem. At present, graphite anodes used in commercial LIBs still suffer many issues, such as low



capacity, poor rate performance and obvious safety issues caused by the low operating voltage (~ 0.1 V (vs. Li/Li^+)) [6, 7]. Therefore, great effort has been devoted to exploring advanced anode materials with high capacity, good rate capability and long cycling stability to replace the graphite anodes [8].

Recently, Li_3VO_4 (LVO) has been reported as a new insertion-type of alternate anodes for high energy density LIBs. LVO exhibits a safe working voltage (0.5–1.0 V (vs. Li/Li^+)) [9, 10], which is higher than that of commercial graphite (~ 0.1 V (vs. Li/Li^+)) and lower than that of $\text{Li}_4\text{Ti}_5\text{O}_{12}$ (~ 1.5 V (vs. Li/Li^+)) [11, 12]. The theoretical specific capacity can reach $394 \text{ mAh}\cdot\text{g}^{-1}$ in shallow discharge ($x = 2$ in $\text{Li}_{3+x}\text{VO}_4$) [13], while a theoretical gravimetric capacity of $594 \text{ mAh}\cdot\text{g}^{-1}$ can be obtained corresponding to $x = 3$ in $\text{Li}_{3+x}\text{VO}_4$ [11]. In addition, the supply of vanadium resources is abundant and the cost is rather low so that LVO has the potential for mass production for enterprises. Although LVO exhibits good phase reversibility and high capacity, many issues should be addressed before obtaining desired electrochemical performances. The poor electronic conductivity ($< 1 \times 10^{-10} \text{ S}\cdot\text{m}^{-1}$) [14] and large volume expansion (20%, corresponding to 3 Li^+ insertion) hinder its power capability and long-term cycling stability [15].

Making carbonaceous composite with active material has been proven to be the most effective strategy to alleviate volume expansion and simultaneously enhance electron conductivity [16–19]. Many LVO/C composites have been synthesized with improved electrochemical performances. Zhang et al. [20] reported a sol–gel method for the synthesis of hollow LVO/C microcuboid composites. The resulting unique hollow LVO/C microcuboid composite exhibited a high capability of $481 \text{ mAh}\cdot\text{g}^{-1}$ at 0.1C. Xu et al. [21] reported a LVO nanoparticle in N-doped carbon with porous structure synthesized via a freeze-drying process. This composite delivers a capacity of $405.1 \text{ mAh}\cdot\text{g}^{-1}$ at 0.1 $\text{A}\cdot\text{g}^{-1}$ and $199.9 \text{ mAh}\cdot\text{g}^{-1}$ at 10 $\text{A}\cdot\text{g}^{-1}$ within 0.2–3.0 V. More recently, double-carbon-based composites have been proposed to further optimizing the electron transportation and lithium-ion diffusion behavior. LVO/C/rGO composite prepared by spray-drying process demonstrates high specific capacity and outstanding cyclability [11], in which double-carbon matrix (rGO and amorphous carbon) greatly enhances the electrical conductivity and accommodates the volume variation of LVO nanoparticles. However, most of the reported experimental strategies are not conducive to large-scale production. Thus, more concise and universal methods need to be further proposed.

Herein, a porous carbon supported Li_3VO_4 composites ($\text{Li}_3\text{VO}_4/\text{C}$) through a facile agitation-drying method combined with subsequent calcination was reported, in which Ketjen black carbon (referred to as KB carbon

hereafter) functions used as one of carbon sources due to its low cost, high porosity, easy dispersion and good electrical conductivity [22]. Detailed investigations on the synthesis condition of the $\text{Li}_3\text{VO}_4/\text{C}$ composites were conducted. The as-prepared $\text{Li}_3\text{VO}_4/\text{C}$ composites exhibit good cycling stability and excellent rate capability, which can be promising alternative anode material for high energy density lithium-ion batteries.

2 Experimental

2.1 Material synthesis

2.1.1 Synthesis of VOC_2O_4

In a typical agitation synthesis process, VOC_2O_4 was prepared according to our previous work [23]. 1.2 g V_2O_5 and $\text{H}_2\text{C}_2\text{O}_4\cdot 2\text{H}_2\text{O}$ (molar ratio of 1:3) were added to 40 ml of deionized (DI) water, and continuous magnetic stirring was performed at 80 °C until a clear blue solution was formed.

2.1.2 Synthesis of LVO/KB carbon

The LVO/KB carbon precursor was synthesized via a facile liquid absorption method. First, 0.404 g (3.96 mmol) of $\text{CH}_3\text{COOLi}\cdot 2\text{H}_2\text{O}$ was dissolved in 40 ml of DI water and then gradually added into 3.64 ml (1.2 mmol) of as-prepared VOC_2O_4 . After that, 0.0067 g KB carbon was added and sonicated for 1 h to disperse the agglomerated parts until a uniform suspension was formed. The suspension was stirred overnight at 80 °C until the water was completely evaporated. The precursor was calcined under an argon atmosphere for 3 h at a heating rate of 3 °C $\cdot\text{min}^{-1}$ to prepare $\text{Li}_3\text{VO}_4/\text{C}$ composites. LVO samples with various KB carbon addition (0%, 5%, 10% and 20%) and calcined at 650 °C, 700 °C and 750 °C were prepared. The samples were noted as LVO-700, LVO5%-700, LVO10%-700, LVO20%-700, LVO10%-650 and LVO10%-750, respectively.

2.2 Material characterization

The crystalline structures of all $\text{Li}_3\text{VO}_4/\text{C}$ composites were investigated by X-ray diffraction (XRD, Rigaku D/max 2500) with $\text{Cu K}\alpha$ radiation collected in the range of 10°–80° at a scanning rate of 8 (°) $\cdot\text{min}^{-1}$. X-ray photoelectron spectroscopy (XPS) was undertaken using an ESCALAB 250Xi to further analyze the surface chemistry of samples. The morphology and microstructures of the samples were characterized by field emission scanning electron microscopy (FESEM, FEI Nova NanoSEM 230, 10 kV) and

transmission electron microscopy (TEM, FEI Tecnai G2 F20, 200 kV). Raman spectrometer (LabRAM HR800) was used to obtain the carbon coating information. Thermogravimetric (TG) analysis was performed on a NETZSCH STA 449C simultaneous thermal analyzer with a heating rate of $10\text{ }^{\circ}\text{C}\cdot\text{min}^{-1}$ in air to determine the carbon contents of the samples. Nitrogen adsorption–desorption isotherms were conducted on a micromeritics analyzer (Micromeritics ASAP 2460, USA) and surface area was calculated according to Brunauer–Emmett–Teller (BET) method.

2.3 Electrochemical measurement

The electrochemical performance of $\text{Li}_3\text{VO}_4/\text{C}$ composites was evaluated by assembling 2016 coin cells through the typical method. The anode slurry was prepared by mixing the active materials (80 wt%), Super-P carbon (10 wt%) and sodium carboxymethyl cellulose (CMC, 10 wt%) binder in DI water. The working electrodes were prepared by applying the slurry onto copper foil by the doctor blading technique and dried in a vacuum oven at $90\text{ }^{\circ}\text{C}$ overnight. The electrodes were cut into circular pieces with diameter of 12 mm. The average mass loading of the active material was $\sim 1\text{ mg}\cdot\text{cm}^{-2}$ (based on the weight of $\text{Li}_3\text{VO}_4/\text{C}$ composites) for the electrodes. All the cells were assembled in a glove box (Mbraun, Germany) filled with high purity argon with an oxygen and water content less than 1×10^{-7} . The lithium metal foils served as counter electrodes, $1\text{ mol}\cdot\text{L}^{-1}$ LiPF_6 in a mixture of ethyl carbonate (EC), dimethyl carbonate (DMC) and diethyl carbonate (DEC) (1:1:1 in volume) works as the electrolyte, and polypropylene membrane was used as the separator. The galvanostatic discharge/charge measurements of the electrodes were performed using a multichannel battery test system (LAND CT2001A, Wuhan Kingnuo Electronic Co., China) in the voltage range between 0.01 and 3 V (vs. Li/Li^+) at room temperature. Cyclic voltammetry (CV, 0.01–3 V) tests were carried out on an electrochemical workstation (CHI660E, China) at various scanning rates from 0.1 to $2\text{ mV}\cdot\text{s}^{-1}$. The electrochemical impedance spectroscopy (EIS) was performed using Zahner electrochemical workstation (IM6ex, Germany) in the frequency range of 0.01 Hz to 100 kHz, with an applied AC voltage amplitude of 5 mV.

3 Results and discussion

Figure 1 illustrates the synthesis process of $\text{Li}_3\text{VO}_4/\text{C}$ composites. VOC_2O_4 and $\text{CH}_3\text{COOLi}\cdot 2\text{H}_2\text{O}$ were firstly dissolved in DI water working as vanadium source and lithium source, respectively. Different masses of KB carbon, which function as carbon sources were subsequently

added to the prepared solution. After stirring for 5 min, a long-time sonication was conducted to completely disperse KB carbon. The obtained suspension was evaporated via agitation-drying overnight to entirely remove the moisture. The prepared precursor was calcined in a tube furnace under the protection of argon to obtain the final $\text{Li}_3\text{VO}_4/\text{C}$ composites. In this process, the VOC_2O_4 and KB carbon are simultaneously used as carbon sources to form the nanoscale amorphous carbon coating and a microscale carbon network, respectively, along with the in situ crystallization of LVO.

The powder XRD patterns collected on $\text{Li}_3\text{VO}_4/\text{C}$ composites are illustrated in Fig. 2a. All the samples show intense and sharp diffraction peaks suggesting the good crystallinity of the as-synthesized composites. Diffraction peaks located at 16.3° , 21.5° , 22.8° , 24.3° , 28.1° , 32.7° , 32.8° , 35.9° , 36.3° , 37.5° , 37.7° , 58.6° correspond to the (100), (110), (011), (101), (111), (120), (200), (210), (002), (121), (201), (320) planes of orthorhombic Pnm21 LVO phase (JCPDS No. 38–1247), with no evidence of secondary phases, indicating the high purity of the as-synthesized samples. It is worth mentioning that the peak intensity increases along with calcination temperature. The full width at half maximum (FWHM) of the several main XRD peaks of LVO10%-650 is larger than that of LVO10%-700 (Table S1, Supporting Information), indicating that the calcination temperature has a significant effect on crystallinity [24, 25].

Raman spectroscopy was used to further investigate the structural information of $\text{Li}_3\text{VO}_4/\text{C}$ composites (Fig. 2b). Two distinct characteristic peaks at ~ 1323 and 1598 cm^{-1} are associated to the D-band of disordered carbon and the G-band of graphitic carbon, respectively. The I_D/I_G (peak intensity ratio between D- and G-bands) indicates the degree of crystallinity for various carbon materials, i.e., the smaller the I_D/I_G ratio is, the better crystallinity of the carbon material is. In this work, the intensity ratios of D/G bands (I_D/I_G) of the three samples are 1.22, 1.07 and 1.04, respectively, suggesting the high-density lattice distortion and structural defects of the carbon layer, which is beneficial to the transport of lithium ions [26]. Moreover, the characteristic peaks of LVO are also detected. The sharp peak located at 814 cm^{-1} is assigned to the symmetric stretching of VO_4^{3-} , while the peak at 783 cm^{-1} is attributed to the asymmetric stretching of VO_4^{3-} [27]. The peak at 369 cm^{-1} is generated by vibration of the VO_4 tetrahedron [28]. The same characteristic peak positions of pure LVO (Fig.S1) further indicate the absence of heterogeneous phases.

TG analysis was performed to investigate the mass content of carbon in $\text{Li}_3\text{VO}_4/\text{C}$ composites. The results from Fig. 2c show that when the temperature rises from room temperature to $700\text{ }^{\circ}\text{C}$ at a rate of $10\text{ }^{\circ}\text{C}\cdot\text{min}^{-1}$ in the

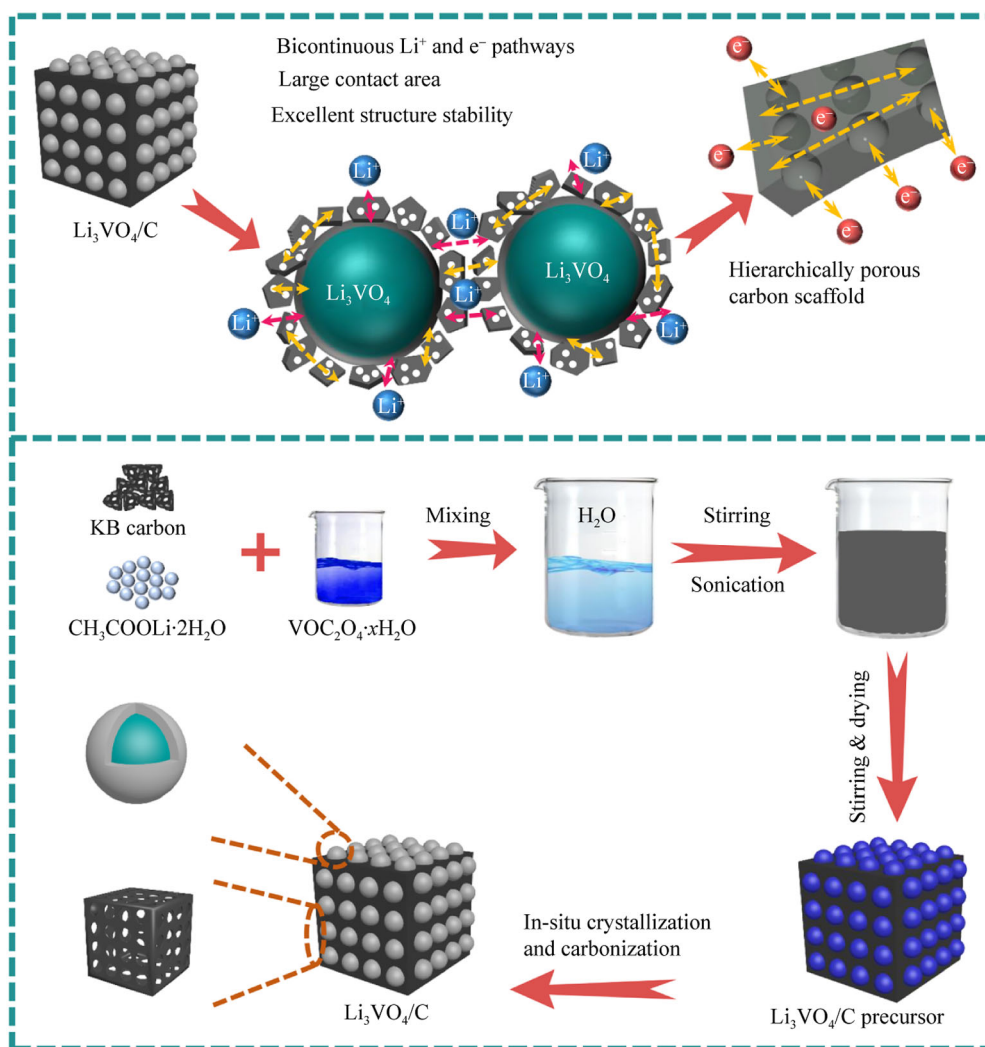


Fig. 1 Schematic illustration for hierarchical carbon decorated Li_3VO_4 with bi-continuous electron/ion pathways and fabrication process of $\text{Li}_3\text{VO}_4/\text{C}$ composites

air, the initial slight decrease in the curves is due to the evaporation of moisture adsorbed on the surface of the samples. The decrease in the curves from 350 to 500 °C is attributed to the pyrolysis of the carbon moieties in the composites, and the final quality remains stable owing to the burning out of carbon. The results show that the mass fractions of carbon in LVO5%-700, LVO10%-700 and LVO20%-700 are 3 wt%, 10.8 wt% and 17 wt%, respectively. The lower mass fraction of KB carbon than theoretical value can be attributed to the loss of carbon during the stirring process. While for LVO10%-700, the higher carbon content can be attributed to the conversion of carbon from VOC_2O_4 . TG profile of pure LVO-700 was performed to measure contribution of this part of carbon. As shown in Fig.S2, contribution of VOC_2O_4 in carbon content is calculated to be ~ 1.8 wt%.

Nitrogen adsorption–desorption isotherms were measured to study the physical adsorption behaviors of $\text{Li}_3\text{VO}_4/\text{C}$ composites. As shown in Fig. 2d, an apparent hysteresis loop is obtained. The BET surface area and average pore volume of LVO10%-700 are calculated to be $39.6 \text{ m}^2\cdot\text{g}^{-1}$ and $0.09 \text{ cm}^3\cdot\text{g}^{-1}$, respectively. Based on the Barrett–Joyner–Halenda (BJH) model (inset of Fig. 2d), the pore size is mainly distributed from 1.7 to 50.0 nm. The high surface area and pore size distribution suggest that the prepared samples will be beneficial to electrolyte penetration and Li ions transfer [29]. Furthermore, BET surface areas of pure LVO-700, LVO5%-700, and LVO20%-700 were tested for comparison, the results are shown in Fig.S3. The specific surface areas of the three samples are 8.3, 21.9 and $74.8 \text{ m}^2\cdot\text{g}^{-1}$, respectively. The same pore size distribution and increasing specific surface area along with

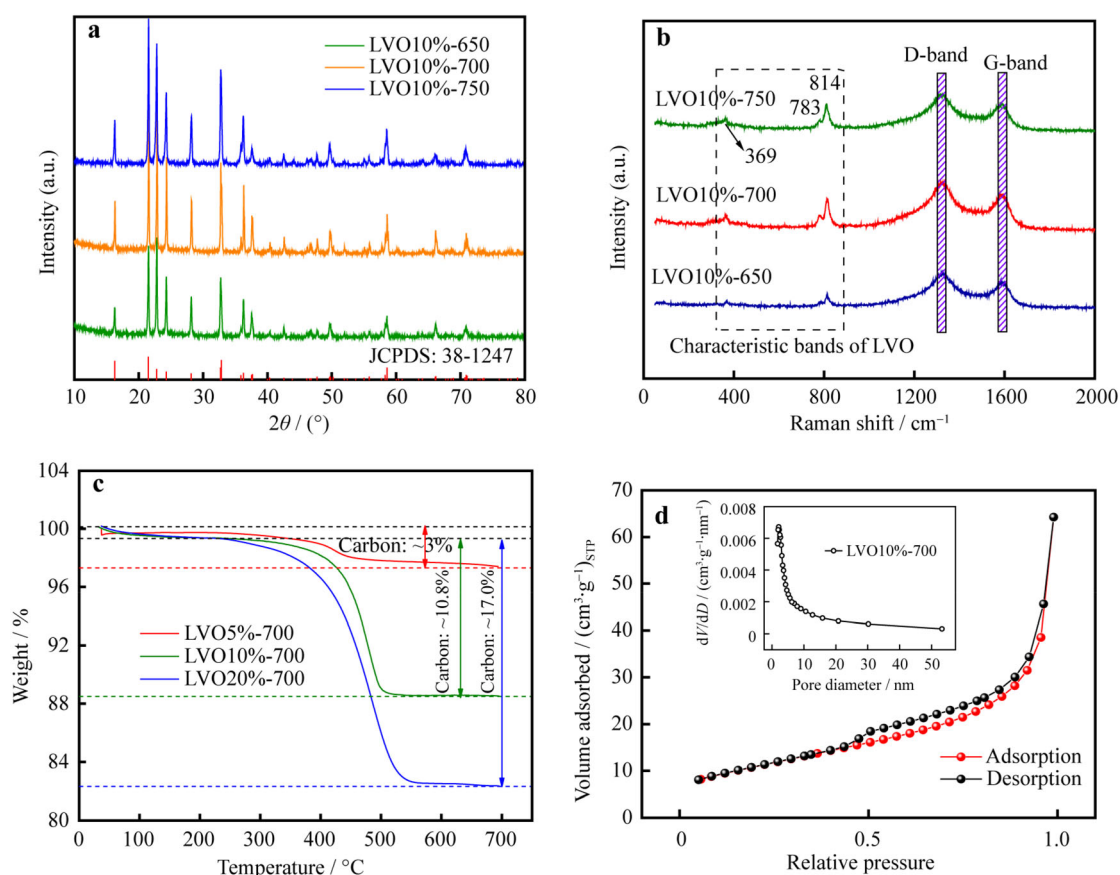


Fig. 2 Characterizations of LVO10%-700 and control samples: **a** XRD patterns; **b** Raman scattering spectra of $\text{Li}_3\text{VO}_4/\text{C}$ composites calcined at different temperatures with a carbon content of $\sim 10\%$; **c** TG profiles of $\text{Li}_3\text{VO}_4/\text{C}$ composites with different KB carbon additions; **d** nitrogen adsorption/desorption isotherm and corresponding pore size distribution curve (inset) of LVO10%-700

carbon content indicate that the porous structure is mainly inherited from KB carbon [30].

The effect of KB carbon on morphology of as-prepared samples was investigated. SEM images of as-synthesized $\text{Li}_3\text{VO}_4/\text{C}$ composites and pure LVO are shown in Figs. 3a, S4. The pure LVO presents non-uniform bulk particles with the diameter of $\sim 0.5\text{--}3.0\ \mu\text{m}$. Fig. S5 shows SEM images of as-prepared LVO5%-700 at different magnifications, a small block morphology can be clearly detected, which is consistent with pure LVO. Although the adhesion of KB carbon on the blocks can be clearly seen, most of the LVO particles are in a bare state. In comparison, as shown in Fig. 3a, LVO blocks are uniformly surrounded by KB carbon in LVO10%-700. The nanoparticles are stacked on each other, bare particles can hardly be found, indicating that LVO and KB carbon are well combined. In addition, according to the SEM images, the nanocomposites exhibit distinct porous structures, which is very important for electrolyte infiltration [31]. The SEM images of LVO20%-700 composite are shown in Fig. S6, which present similar morphology with LVO10%-700 composite, however, the content of KB carbon is significantly increased.

TEM observation was further conducted to determine the detailed structural information of the crystals (Fig. 3b, c). It is clear that the size of LVO particles is $\sim 50\ \text{nm}$, which are uniformly distributed in the amorphous KB carbon matrix, with good contact characteristics. The high-resolution TEM (HRTEM) images in Fig. 3d, e clearly show the amorphous carbon layer and lattice fringes with an interplanar spacing of 0.27 and 0.41 nm, corresponding to the (200) and (110) crystal planes of orthorhombic LVO. The carbon layer coated on the surface of LVO nanocrystals can effectively improve the charge transfer, alleviate the volume variations during repeated Li ion insertion and extraction. The high-angle annular dark field (HAADF) image (Fig. 3f) and corresponding elemental mappings (Fig. 3g–i) of LVO10%-700 intuitively display that V and O are homogeneously distributed throughout the carbon matrix, which indicates the uniform dispersion of LVO through the carbon framework.

XPS was employed to detect the surface elemental composition and detailed chemical state of as-prepared LVO10%-700. The XPS survey spectrum of LVO10%-700, as shown in Fig. 4a, demonstrates that only Li, C, V

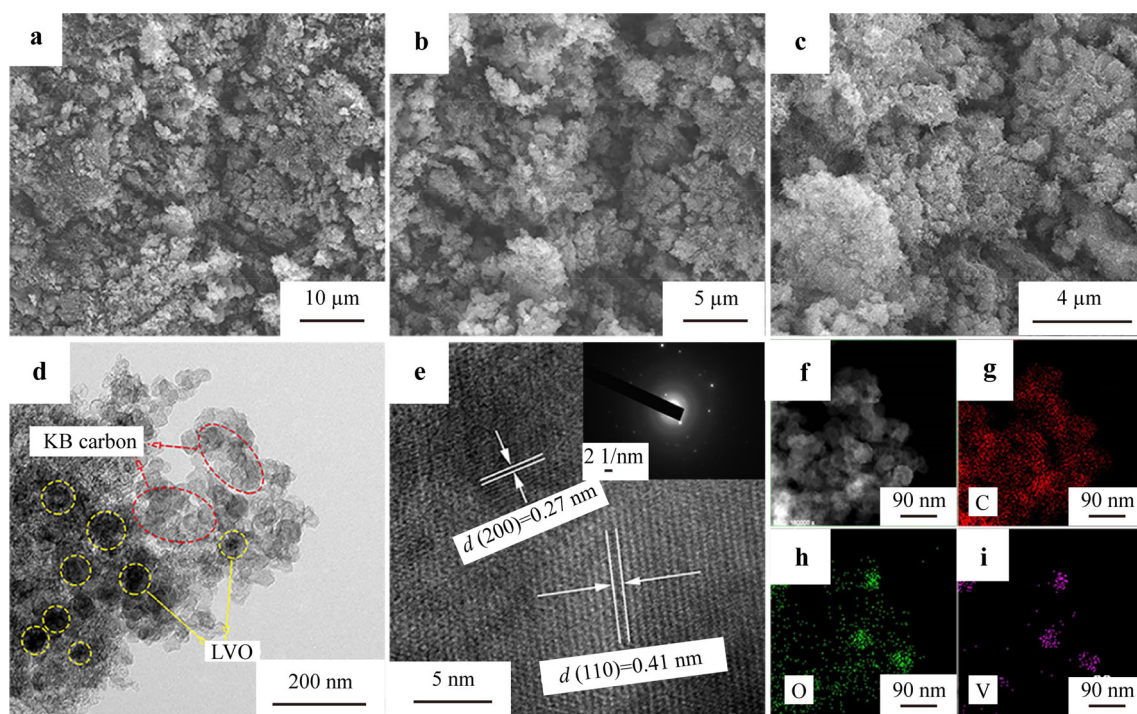
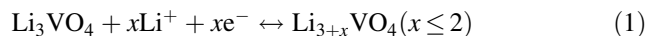


Fig. 3 Morphology and structure characterizations of LVO10%-700: **a** SEM image; **b**, **c** TEM images; **d**, **e** HRTEM images and corresponding SAED pattern (inset of **e**); **f** STEM-HAADF image and **g**–**i** corresponding elemental mappings

and O elements exist in the composite. The high-resolution spectrum of C 1s (Fig. 4b) can be divided into three peaks located at 284.8, 285.8 and 290.2 eV, respectively, corresponding to C–C bond, C–O bond and O–C=O bond [32]. The dominant peak is derived from KB carbon of the composite, while C–O bond and O–C=O bond are from CO_2 adsorbed on the surface of the sample. The O 1s spectrum is displayed in Fig. 4c, two main peaks located at 530.9 and 532.6 eV can be resolved, which can be assigned to O–Li/O = V bonds and O adsorbed on the surface [33]. XPS spectra of V 2p are deconvoluted, and the fitting result is shown in Fig. 4d, the peaks at 517.9 and 518.7 eV can be indexed to $\text{V}^{5+} 2\text{P}_{3/2}$, and the peaks at 524.2 and 525.9 eV belong to $\text{V}^{5+} 2\text{P}_{1/2}$ [34].

The lithium storage performance of the $\text{Li}_3\text{VO}_4/\text{C}$ composites was investigated by assembling half-cells. Figure 5a shows the initial three CV curves of LVO10%-700 working as the anode material for LIBs at a scan rate of $0.1 \text{ mV}\cdot\text{s}^{-1}$. In the first cathode scan, a significant reduction peak appeared at $\sim 0.37 \text{ V}$, which disappeared in the subsequent scans, which can be assigned to the formation of solid electrolyte interphase (SEI) film [6]. From the second lap, two main reduction peaks located at ~ 0.52 and 0.95 V appeared in the following cycles, which represent the phase transformation to $\text{Li}_{3+x}\text{VO}_4$ ($x \leq 2$) along with the reduction of V^{5+} to V^{4+} and V^{4+} to V^{3+} , respectively. Two distinct oxidation peaks appeared at ~ 1.11 and 1.38 V reveal the delithiation process from

V^{3+} to V^{4+} and V^{4+} to V^{5+} in the anode scan [35]. The second CV curve approximately overlaps with the third cycle, indicating excellent reversibility and cycle performance. Based on the above facts, the reaction of insertion and deinsertion of $\text{Li}_3\text{VO}_4/\text{C}$ composite during charge and discharge can be described by the following equation [9]:



The galvanostatic charge–discharge cycle test was carried out to evaluate the electrochemical performance of the $\text{Li}_3\text{VO}_4/\text{C}$ composites. Figure 5b shows the charge–discharge curves of LVO10%-700 at a current density of $100 \text{ mA}\cdot\text{g}^{-1}$ between 0.01 and 3 V (vs. Li/Li^+). The result shows that during the first discharge, there is a relatively obvious voltage plain 0.37–0.77 V and gradually shifts to 0.5 and 0.9 V during the subsequent discharge process, which is completely consistent with the CV curves. In addition, the discharge capacity of the first circle is $636.8 \text{ mAh}\cdot\text{g}^{-1}$, and corresponding charge specific capacity is $435.7 \text{ mAh}\cdot\text{g}^{-1}$, declaring a coulombic efficiency of 68.4%. The loss of capacity mainly comes from irreversible and side reactions, including the decomposition of electrolyte and the formation of SEI film. The charge and discharge curves from 2nd to 50th cycles substantially coincide, indicating good reversibility.

To explore the effect of carbon content and calcination temperature on the electrochemical performance of the composites, pure LVO-700, LVO5%-700, LVO10%-700

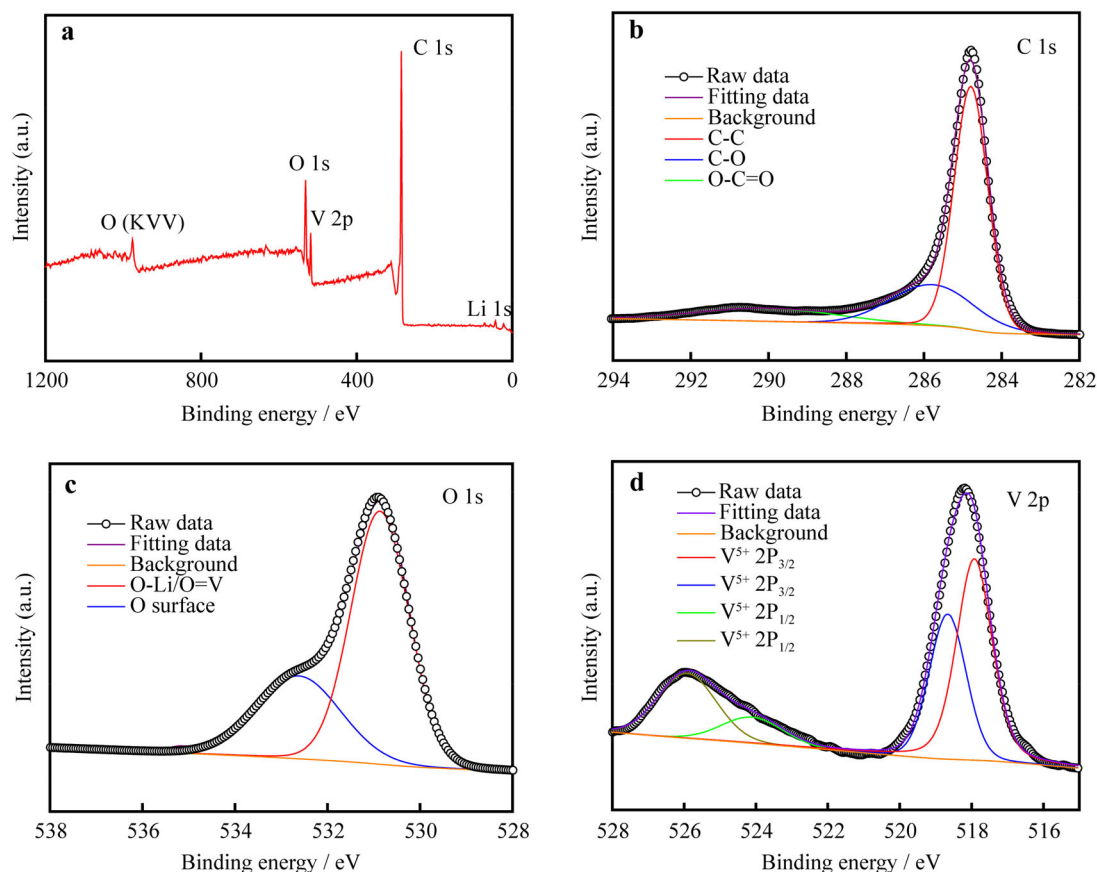


Fig. 4 a Typical XPS survey spectrum and corresponding: b C 1s, c O 1s, and d V 2p spectra for LVO10%-700 sample

and LVO20%-700 were assembled into half-cells to evaluate their electrochemical performances as anode materials for LIBs. The cycling performance in Fig. 6a shows that LVO10%-700 exhibits the highest discharge capacity of $572 \text{ mAh}\cdot\text{g}^{-1}$ and maintains a discharge specific capacity of $442.9 \text{ mAh}\cdot\text{g}^{-1}$ after 100 cycles, showing the best cyclic stability among the $\text{Li}_3\text{VO}_4/\text{C}$ composites with different KB carbon additions. It should be noted that the low initial coulombic efficiency may be ascribed to the decomposition of electrolyte and the formation of SEI film and oxygen-containing functional group of carbon. Rate performance of the four samples was conducted to further evaluate the electrochemical performance, the result is shown in Fig. 6b. Obviously, LVO10%-700 exhibits the optimal rate behavior, which is consistent with the cycle consequence. The discharge capacities of 426.2 , 400.3 , 367.7 , 329.7 , 292.4 and $243.8 \text{ mAh}\cdot\text{g}^{-1}$ are obtained at a current density of 50 , 100 , 200 , 500 , 1000 and $2000 \text{ mA}\cdot\text{g}^{-1}$. Notably, when current density is reset to $50 \text{ mA}\cdot\text{g}^{-1}$, the obtained capacity recovers to $412.8 \text{ mAh}\cdot\text{g}^{-1}$, revealing good reversibility. To sum up, the as-prepared LVO composite with 10% KB carbon shows the best electrochemical performance at the same calcination temperature based on above facts.

Temperature greatly affects the crystallinity of the materials as well as the combination of LVO and KB carbon. The electrochemical properties of $\text{Li}_3\text{VO}_4/\text{C}$ composites calcined at different temperatures (noted as LVO10%-650, LVO10%-700 and LVO10%-750) are also investigated. Obviously, LVO10%-700 displays the highest discharge specific capacity with good cyclic stability (Fig. 6c) as well as the rate performance (Fig. 6d). It can be concluded that the $\text{Li}_3\text{VO}_4/\text{C}$ composite with a KB carbon content of 10% exhibits the best electrochemical performance when calcined at 700°C in Ar atmosphere. Under this optimized parameter, LVO10%-700 composite has a hierarchical carbon decorating structure, larger surface area and pore volume combined with suitable carbon content, which is the key to the excellent electrochemical performance. The electrochemical performance of $\text{Li}_3\text{VO}_4/\text{C}$ composite is better than many reported Li_3VO_4 anodes (Table S2).

To gain insights on electrochemical reaction kinetics, EIS was performed (Fig. 7). Based on the equivalent circuit model in inset of the Fig. 7, the R_s is the combination of electrolyte resistance and Ohmic resistances of cell components. The Nyquist plots of pure LVO-700, LVO5%-700, LVO10%-700 and LVO20%-700 are

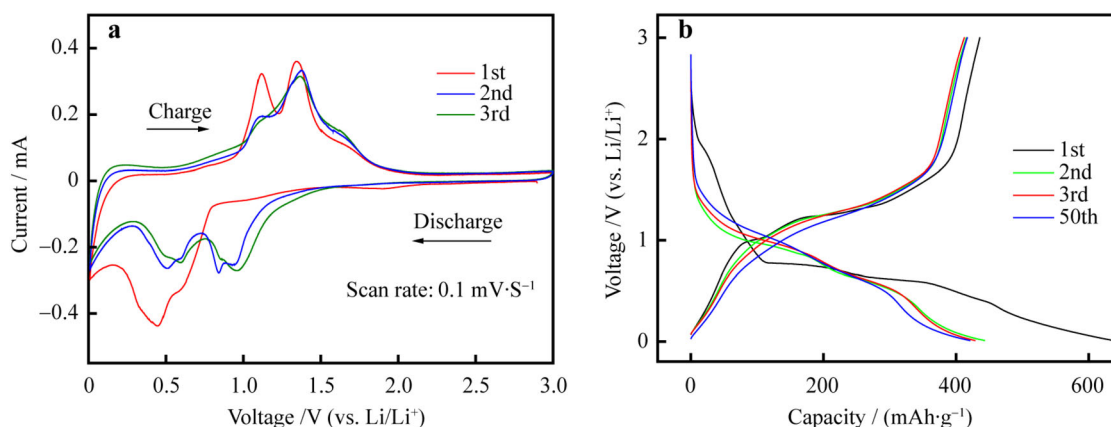


Fig. 5 a Initial three CV curves of LVO10%-700 electrode at scan rate of $0.1 \text{ mV}\cdot\text{s}^{-1}$; b typical discharge-charge voltage profiles of LVO10%-700 electrode at current density of $100 \text{ mA}\cdot\text{g}^{-1}$

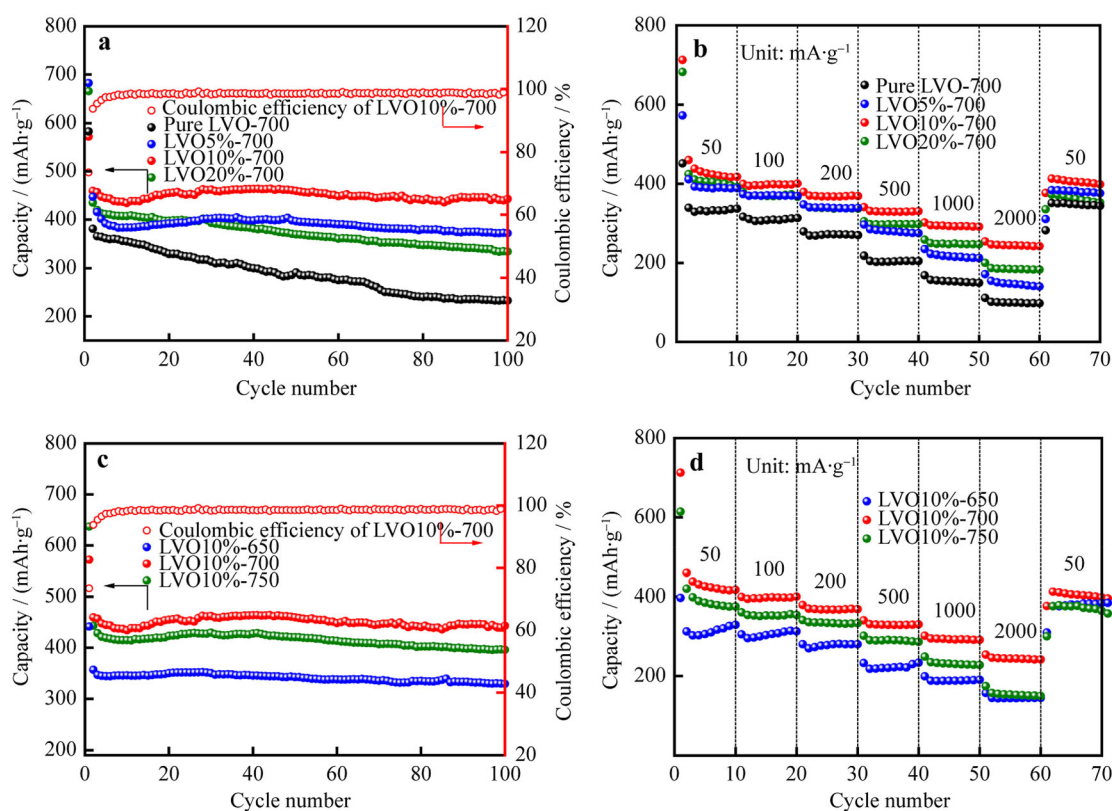


Fig. 6 Electrochemical performance of $\text{Li}_3\text{VO}_4/\text{C}$ composites for lithium storage: a cycling performance at current density of $100 \text{ mA}\cdot\text{g}^{-1}$; b rate performance at various current densities of $\text{Li}_3\text{VO}_4/\text{C}$ composites with different KB carbon additions; c cycling performance at current density of $100 \text{ mA}\cdot\text{g}^{-1}$; d rate performance at various current densities of $\text{Li}_3\text{VO}_4/\text{C}$ composites calcined at different temperatures with a carbon content of $\sim 10\%$

composed of a semicircle in the high frequency region and a sloping line in the low frequency region corresponding to charge transfer resistance (R_{ct}) and the Warburg impedance (Z_w), respectively. The semicircle is mainly ascribed to the charge transfer reaction, and the slanted line is ascribed to the diffusion process of Li ions in the bulk of the electrode material. According to

the results of the equivalent circuit diagram simulation (the inset), the simulated charge transfer resistances of pure LVO-700, LVO5%-700, LVO10%-700 and LVO20%-700 are 705, 347, 170 and 303 Ω , respectively. The smallest R_{ct} indicates the superior interfacial stability and charge transfer kinetics of LVO10%-700, which is consistent with the cycling tests.

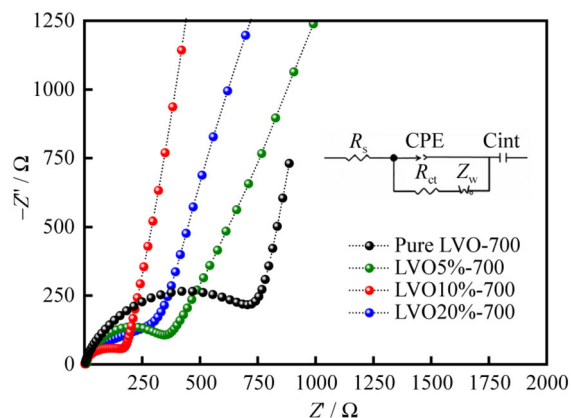


Fig. 7 Nyquist plots of $\text{Li}_3\text{VO}_4/\text{C}$ composites with different KB carbon additions and corresponding equivalent circuit diagram simulation (inset), where Z' is real part of impedance, Z'' is imaginary part of impedance

The CV tests of LVO10%-700 at different scan rates were performed to analyze the kinetics of the half-cells. Figure 8a shows the typical CV curves at various scan rates from 0.1 to 2.0 $\text{mV}\cdot\text{s}^{-1}$. The oxidation peaks gradually

shift to the high potential region, while the positions of the reduction peaks shift to the low potential region along with the increasing in scan rates, which is a polarization phenomenon exhibited by the electrode at a high sweep speed. Generally, the relationship between current peak (i) and the scan rate (v) can be described by equations as follows [36]:

$$i = av^b \quad (2)$$

$$\lg i = b \lg v + \lg a \quad (3)$$

where a and b are adjustable values, b value can be determined by the slope of the fitted line through plotting $\lg v$ and $\lg i$. $b = 0.5$ represents the ideal ion diffusion process, while $b = 1$ refers to the ideal pseudocapacitive process [37]. Figure 8b shows the $\lg i$ - $\lg v$ plot of oxidation peak in which the b value is calculated to be 0.8, indicating a combination of the above two behaviors during charging and discharging. According to previous reports, the ion diffusion process and the contribution of pseudocapacitive to Li ion storage can be further quantified. Current i at a permanent potential can be expressed as:

$$i = k_1 v + k_2 v^{0.5} \quad (4)$$

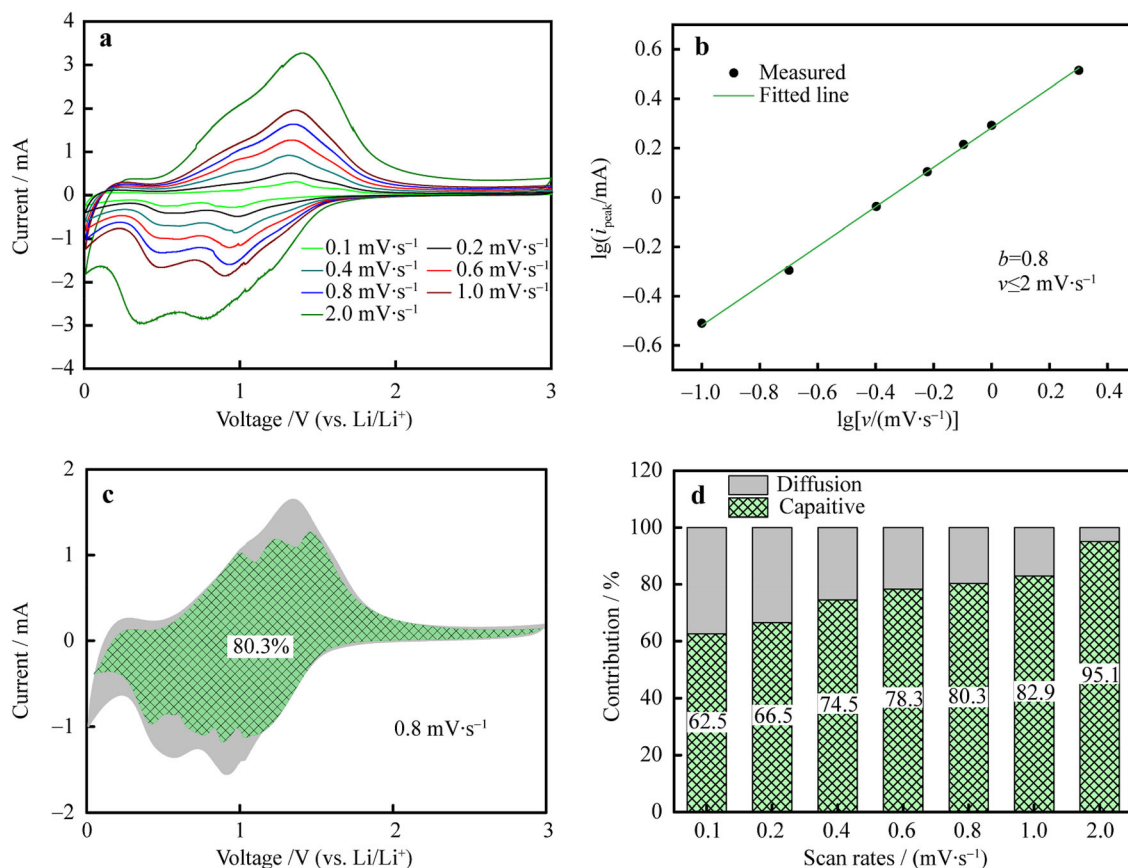


Fig. 8 a CV curves of LVO10%-700 electrode at various scan rates from 0.1 to 2.0 $\text{mV}\cdot\text{s}^{-1}$; b determination of b value using relationship between peak current and scan rate; c separation of capacitive and diffusion currents in LVO10%-700 electrode at scan rate of 0.8 $\text{mV}\cdot\text{s}^{-1}$ with capacitive fraction shown by shaded region; d contribution ratio of capacitive and diffusion-controlled charge versus scan rate

where k_1v and $k_2v^{0.5}$ represent the contribution as a result of pseudocapacitive and ion diffusion, respectively [38]. Figure 8c displays the contribution of pseudocapacitive (the shadow area) at a scan rate of $0.8 \text{ mV}\cdot\text{s}^{-1}$, 80.3% of the stored charge arises from pseudocapacitive processes. The same calculation method is conducted to obtain the contributions of pseudocapacitive under different sweep rates, the result is shown in Fig. 8d (histogram), revealing the capacitance contributions of pseudocapacitive at sweep rates of 0.1, 0.2, 0.4, 0.6, 0.8, 1.0 and $2.0 \text{ mV}\cdot\text{s}^{-1}$ are 62.5%, 66.5%, 74.5%, 78.3%, 80.3%, 82.9% and 95.1%, respectively. The kinetic analysis demonstrates that the slower ion embedding mechanism hardly satisfy the rapid electrochemical reaction with the increase in scan rate. The charge storage is greatly related to the pseudocapacitive process, which is beneficial to the rapid storage of charge, long-term cycling, and excellent rate performance of LVO10%-700 electrode.

4 Conclusion

In summary, the hierarchical porous carbon decorated LVO composites were successfully synthesized via a facile agitation-drying method combined with subsequent heat treatment. The effects of carbon content and calcination temperature on structure and electrochemical properties of the LVO composites were studied in detail. The product (LVO10%-700) exhibits the best electrochemical performance with a KB carbon addition of 10% and calcined at 700°C in the Ar, which possesses a high initial specific capacity of $572 \text{ mAh}\cdot\text{g}^{-1}$ and maintains a discharge capacity of $442.9 \text{ mAh}\cdot\text{g}^{-1}$ after 100 cycles. This excellent electrochemical performance may be attributed to the optimal hierarchical carbon decorated architecture, which provides effective electrode–electrolyte contact area, shortened ion diffusion distance and rapid electron transport. This strategy can easily be scaled up for commercialization and provides a considerable reference value for the practical application of LVO as anode material for LIBs.

Acknowledgements This work was financially supported by the National Natural Science Foundation of China (Nos. 51874362 and 51872334), the Natural Science Foundation of Hunan Province, China (No. 2018JJ1036), the National Key Research and Development Program of China (No. 2018YFB0104200).

References

- [1] Wang YY, Zhao ZW, Liu Y, Hou LR, Yuan CZ. Precipitant-free solvothermal construction of spindle-like $\text{CoCo}_3/\text{reduced}$ graphene oxide hybrid anode toward high-performance lithium-ion batteries. *Rare Met.* 2020;39(9):1082.
- [2] Wu ZH, Yang JY, Yu B, Shi BM, Zhao CR, Yu ZL. Self-healing alginate-carboxymethyl chitosan porous scaffold as an effective binder for silicon anodes in lithium-ion batteries. *Rare Met.* 2019;38(9):832.
- [3] Cao XX, Zhou J, Pan AQ, Liang SQ. Recent advances in phosphate cathode materials for sodium-ion batteries. *Acta Phys-Chim Sin.* 2020;36(5):1905018.
- [4] Sari MKH, Li XF. Controllable cathode-electrolyte interface of $\text{Li}[\text{Ni}_{0.8}\text{Co}_{0.1}\text{Mn}_{0.1}]\text{O}_2$ for lithium ion batteries a review. *Adv Energy Mater.* 2019;9(39):1901597.
- [5] Zheng SQ, Wu ZH, Wang JT, Zhang XJ. Performance of high capacity silicon/carbon anodes with different pore structures. *Chin J Rare Metals.* 2020;44(03):225.
- [6] Park H, Jae W, Kim J. One-pot synthesis of Li_3VO_4 particles with thin nitrogen-doped carbon coating layers as an anode material for lithium-ion batteries. *J Alloy Compd.* 2018;767:657.
- [7] Kong XZ, Zhu T, Cheng FY, Zhu MN, Cao XX, Liang SQ, Cao GZ, Pan AQ. Uniform MnCo_2O_4 porous dumbbells for lithium-ion batteries and oxygen evolution reactions. *ACS Appl Mater Interfaces.* 2018;10(10):8730.
- [8] Kong XZ, Pan AQ, Wang YP, Selvakumaran D, Lin JD, Cao XX, Liang SQ, Cao GZ. In situ formation of porous graphitic carbon wrapped MnO/Ni microsphere networks as binder-free anodes for high-performance lithium-ion batteries. *J Mater Chem A.* 2018;6(26):12316.
- [9] Shen LF, Lv HF, Chen SQ, Kopold P, van Aken PA, Wu XJ, Maier J, Yu Y. Peapod-like $\text{Li}_3\text{VO}_4/\text{N}$ -doped carbon nanowires with pseudocapacitive properties as advanced materials for high-energy lithium-ion capacitors. *Adv Mater.* 2017;29(27):1700142.
- [10] Yang G, Zhang BW, Feng JY, Lu Y, Wang ZQ, Aravindan V, Aravind M, Liu JL, Srinivasan M, Shen ZX, Huang YZ. Morphology controlled lithium storage in Li_3VO_4 anodes. *J Mater Chem A.* 2018;6(2):456.
- [11] Liu HC, Hu P, Yu Q, Liu ZH, Zhu T, Luo W, Zhou L, Mai LQ. Boosting the deep discharging/charging lithium storage performances of Li_3VO_4 through double-carbon decoration. *ACS Appl Mater Interfaces.* 2018;10(28):23938.
- [12] Yi TF, Yang SY, Xie Y. Recent advances of $\text{Li}_4\text{Ti}_5\text{O}_{12}$ as a promising next generation anode material for high power lithium-ion batteries. *J Mater Chem A.* 2015;3(11):5750.
- [13] Shi Y, Wang JZ, Chou SL, Wexler D, Li HJ, Ozawa K, Liu HK, Wu YP. Hollow structured Li_3VO_4 wrapped with graphene nanosheets in situ prepared by a one-pot template-free method as an anode for lithium-ion batteries. *Nano Lett.* 2013;13(10):4715.
- [14] Fu Q, Du F, Bian XF, Wang YH, Yan X, Zhang YQ, Zhu K, Chen G, Wang CZ, Wei YJ. Electrochemical performance and thermal stability of $\text{Li}_{1.18}\text{Co}_{0.15}\text{Ni}_{0.15}\text{Mn}_{0.52}\text{O}_2$ surface coated with the ionic conductor Li_3VO_4 . *J Mater Chem A.* 2014;2(20):7555.
- [15] Arroyo-de Dompablo M, Tartaj P, Amarilla JM, Amador U. Computational investigation of Li insertion in Li_3VO_4 . *Chem Mater.* 2016;28(16):5643.
- [16] Zhang CK, Song HQ, Liu CF, Liu YG, Zhang CP, Nan XH, Cao GZ. Fast and reversible Li ion insertion in carbon-encapsulated Li_3VO_4 as anode for lithium-ion battery. *Adv Funct Mater.* 2015;25(23):3497.
- [17] Li QD, Sheng JZ, Wei QL, An QY, Wei XJ, Zhang PF, Mai LQ. A unique hollow $\text{Li}_3\text{VO}_4/\text{carbon}$ nanotube composite anode for high rate long-life lithium-ion batteries. *Nanoscale.* 2014;6(19):11072.
- [18] Liu J, Lu PJ, Liang SQ, Liu J, Wang WJ, Lei M, Tang SS, Yang Q. Ultrathin Li_3VO_4 nanoribbon/graphene sandwich-like



- nanostructures with ultrahigh lithium ion storage properties. *Nano Energy*. 2015;12:709.
- [19] Cao XX, Pan AQ, Liu SN, Zhou J, Li S, Cao GZ, Liu J, Liang SQ. Chemical synthesis of 3D graphene-like cages for sodium-ion batteries applications. *Adv Energy Mater*. 2017;7(20):1700797.
- [20] Zhang CK, Liu CF, Nan XH, Song HQ, Liu YG, Zhang CP, Cao GZ. Hollow-cuboid $\text{Li}_3\text{VO}_4/\text{C}$ as high-performance anodes for lithium-ion batteries. *ACS Appl Mater Interfaces*. 2016;8(1):680.
- [21] Xu XN, Niu FE, Wang CS, Li YJ, Zhao CL, Yang J, Qian YT. Li_3VO_4 nanoparticles in N-doped carbon with porous structure as an advanced anode material for lithium-ion batteries. *Chem Eng J*. 2019;370:606.
- [22] An XX, Yang HL, Wang YP, Tang Y, Liang SQ, Pan AQ, Cao GZ. Hydrothermal synthesis of coherent porous $\text{V}_2\text{O}_5/\text{carbon}$ nanocomposites for high-performance lithium-and sodium-ion batteries. *Sci China Mater*. 2017;60(8):717.
- [23] Pan AQ, Wu HB, Yu L, Zhu T, Lou XW. Synthesis of hierarchical three-dimensional vanadium oxide microstructures as high-capacity cathode materials for lithium-ion batteries. *ACS Appl Mater Interfaces*. 2012;4(8):3874.
- [24] Uchaker E, Zheng YZ, Li S, Candelaria SL, Hu S, Cao GZ. Better than crystalline: amorphous vanadium oxide for sodium-ion batteries. *J Mater Chem A*. 2014;2(43):18208.
- [25] Xie XF, Hu Y, Fang GZ, Cao XX, Yin B, Wang YP, Liang SQ, Cao GZ, Pan AQ. Towards a durable high performance anode material for lithium storage: stabilizing N-doped carbon encapsulated FeS nanosheets with amorphous TiO_2 . *J Mater Chem A*. 2019;7(27):16541.
- [26] Cao XX, Pan AQ, Zhang YF, Lin JD, Luo ZG, Yang X, Liang SQ, Cao GZ. Nanorod-nanoflake interconnected $\text{LiMnPO}_4\cdot\text{Li}_3\text{V}_2(\text{PO}_4)_3/\text{C}$ composite for high-rate and long-life lithium-ion batteries. *ACS Appl Mater Interfaces*. 2016;8(41):27632.
- [27] Massarotti V, Capsoni D, Bini M, Mustarelli P, Chiodelli G, Azzoni CB, Galinetto P, Mozzati MC. Transport and structural properties of pure and Cr doped Li_3VO_4 . *J Phys Chem B*. 2005;109(31):14845.
- [28] Tao Y, Yi DQ, Li J. Electrochemical formation of crystalline $\text{Li}_3\text{VO}_4/\text{Li}_4\text{SiO}_4$ solid solutions film. *Solid State Ion*. 2008;179(40):2396.
- [29] Yin B, Cao XX, Pan AQ, Luo ZG, Dinesh S, Lin JD, Tang Y, Liang SQ, Cao GZ. Encapsulation of CoS_x nanocrystals into N/S Co-doped honeycomb-like 3D porous carbon for high-performance lithium storage. *Adv Sci*. 2018;5(9):1800829.
- [30] Pan AQ, Liu J, Zhang JG, Xu W, Cao GZ, Nie ZM, Arey BW, Liang SQ. Nano-structured $\text{Li}_3\text{V}_2(\text{PO}_4)_3/\text{carbon}$ composite for high-rate lithium-ion batteries. *Electrochem Commun*. 2010;12(12):1674.
- [31] Zhao YF, Cao XX, Fang GZ, Wang YP, Yang HL, Liang SQ, Pan AQ, Cao GZ. Hierarchically carbon-coated $\text{Na}_3\text{V}_2(\text{PO}_4)_3$ nanoflakes for high-rate capability and ultralong cycle-life sodium ion batteries. *Chem Eng J*. 2018;339:162.
- [32] Cao XX, Pan AQ, Yin B, Fang GZ, Wang YP, Kong XZ, Zhu T, Zhou J, Cao GZ, Liang SQ. Nanoflake-constructed porous $\text{Na}_3\text{V}_2(\text{PO}_4)_3/\text{C}$ hierarchical microspheres as a bicontinuous cathode for sodium-ion batteries applications. *Nano Energy*. 2019;60:312.
- [33] Sathiyam M, Prakash AS, Ramesha K, Tarascon JM, Shukla AK. V_2O_5 -anchored carbon nanotubes for enhanced electrochemical energy storage. *J Am Chem Soc*. 2011;133(40):16291.
- [34] Ni SB, Zhang JC, Ma JJ, Yang XL, Zhang LL, Li XM, Zeng HB. Approaching the theoretical capacity of Li_3VO_4 via electrochemical reconstruction. *Adv Mater Interfaces*. 2016;3(1):1500340.
- [35] Ye JN, Cheng JX, Xiao WQ, Xi L, Xie F, Hu YJ. Constructing Li_3VO_4 nanoparticles anchored on crumpled reduced graphene oxide for high-power lithium-ion batteries. *New J Chem*. 2018;42(16):13241.
- [36] Brezesinski T, Wang J, Polleux J, Dunn B, Tolbert SH. Templated nanocrystal-based porous TiO_2 films for next-generation electrochemical capacitors. *J Am Chem Soc*. 2009;131(5):1802.
- [37] Wang YP, Zhang YF, Shi JR, Kong XZ, Cao XX, Liang SQ, Cao GZ, Pan AQ. Tin sulfide nanoparticles embedded in sulfur and nitrogen dual-doped mesoporous carbon fibers as high-performance anodes with battery-capacitive sodium storage. *Energy Storage Mater*. 2018;18:366.
- [38] Chen J, Pan AQ, Wang YP, Cao XX, Zhang W, Kong XZ, Su Q, Lin JD, Cao GZ, Liang SQ. Hierarchical mesoporous $\text{MoSe}_2@\text{CoSe}/\text{N}$ -doped carbon nanocomposite for sodium ion batteries and hydrogen evolution reaction applications. *Energy Storage Mater*. 2019;21:97.